FLORE
Repository istituzionale dell'Università degli Studi di Firenze

Computational and experimental analysis of supersonic air ejector: Turbulence modeling and assessment of 3D effects

Questa è la versione Preprint (Submitted version) della seguente pubblicazione:

Original Citation:

Computational and experimental analysis of supersonic air ejector: Turbulence modeling and assessment of 3D effects / Mazzelli, Federico; Little, Adrienne B; Garimella, Srinivas; Bartosiewicz, Yann. - In: INTERNATIONAL JOURNAL OF HEAT AND FLUID FLOW. - ISSN 0142-727X. - ELETTRONICO. - 56:(2015), pp. 305-316. [10.1016/j.ijheatfluidflow.2015.08.003]

Availability:

The webpage https://hdl.handle.net/2158/1022728 of the repository was last updated on 2021-03-30T09:05:26Z

Published version:

DOI: 10.1016/j.ijheatfluidflow.2015.08.003

Terms of use:

Open Access

La pubblicazione è resa disponibile sotto le norme e i termini della licenza di deposito, secondo quanto stabilito dalla Policy per l'accesso aperto dell'Università degli Studi di Firenze (https://www.sba.unifi.it/upload/policy-oa-2016-1.pdf)

Publisher copyright claim:

Conformità alle politiche dell'editore / Compliance to publisher's policies

Questa versione della pubblicazione è conforme a quanto richiesto dalle politiche dell'editore in materia di copyright.

This version of the publication conforms to the publisher's copyright policies.

La data sopra indicata si riferisce all'ultimo aggiornamento della scheda del Repository FloRe - The above-mentioned date refers to the last update of the record in the Institutional Repository FloRe

(Article begins on next page)

02 May 2026

COMPUTATIONAL AND EXPERIMENTAL ANALYSIS OF SUPERSONIC AIR EJECTOR: TURBULENCE MODELING AND ASSESSMENT OF 3D EFFECTS

Federico Mazzelli[a], Adrienne B. Little[b], Srinivas Garimella[b], and Yann Bartosiewicz[c]

[a]Department of Industrial Engineering (DIEF)
Università Degli Studi Firenze, Florence, Italy
federico.mazzelli@unifi.it

[b]George W. Woodruff School of Mechanical Engineering
Georgia Institute of Technology, Atlanta, GA, USA
sgarimella@gatech.edu

[c]Institute of Mechanics, Materials, and Civil engineering (iMMC)
Université catholique de Louvain (UCL), Louvain-la-Neuve, Belgium
yann.bartosiewicz@uclouvain.be

ABSTRACT

Numerical and experimental analyses are performed on a supersonic air ejector to evaluate the effectiveness of commonly-used computational techniques when predicting ejector flow characteristics. Three series of experimental curves at different operating conditions are compared with 2D and 3D simulations using RANS, steady, wall-resolved models. Four different turbulence models are tested: *k*-ε, *k*-ε realizable, *k*-ω SST, and the stress-ω Reynolds Stress Model. An extensive analysis is performed to interpret the differences between numerical and experimental results. The results show that while differences between turbulence models are typically small with respect to the prediction of global parameters such as ejector inlet mass flow rates and Mass Entrainment Ratio (MER), the *k*-ω SST model generally performs best whereas ε-based models are more accurate at low motive pressures. Good agreement is found across all 2D and 3D models at

on-design conditions. However, prediction at off-design conditions is only acceptable with 3D models, making 3D simulations mandatory to correctly predict the critical pressure and achieve reasonable results at off-design conditions. This may partly depend on the specific geometry under consideration, which in the present study has a rectangular cross section with low aspect ratio.

1 INTRODUCTION

Supersonic ejectors have long been used as passive pumping devices for a range of applications such as nuclear reactor cooling, pumping of volatile fluids, and compression of refrigerants in energy systems. Superior ejector performance is typically achieved when maximizing the entrainment of a low pressure stream (suction flow) with respect to a certain amount of high pressure flow (motive flow), or in other words, by maximizing the mass entrainment ratio (MER) defined as

$$MER = \frac{\dot{m}_{suction}}{\dot{m}_{motive}} \tag{1}$$

This entrainment effect is the result of momentum transfer between two fluids through a shear-mixing layer inside the ejector, depicted qualitatively in Fig. 1. A high pressure motive flow enters a converging-diverging nozzle where it chokes at the throat and then accelerates to supersonic velocities in the divergent section. The low pressure stream enters the suction nozzle, accelerates slightly, and then reaches the mixing chamber. At this point, mechanical energy is transferred from the supersonic motive stream to the subsonic suction stream through the development of a turbulent mixing layer. Depending on the geometric design and operating conditions, the resulting mixed stream may reach supersonic conditions before exiting the mixing section. The supersonic mixed flow will then adjust to pressure conditions in a succession of oblique shocks [2]. The position of

the shock train depends on the back pressure, where the higher the outlet pressure, the earlier the mixed flow will shock (for very low back pressure, the shock train enters the subsonic diffuser). Downstream of this point, the motive jet becomes subsonic and the pressure increases gradually to the outlet pressure. Under these circumstances (where the suction flow reaches or exceeds sonic velocity), ejector operation is said to be “on-design,” and the suction flow rate is independent of the outlet pressure. On the contrary, if the mixed flow remains subsonic, the amount of suction flow drawn into the ejector depends on the outlet pressure and the operation is said to be “off-design.” The threshold value of outlet pressure between these two operational modes is called the “critical pressure.” Figure 2 shows a characteristic curve of the ejector, generated at a constant motive and suction inlet pressure, and varying outlet pressure. The critical point is indicated at the critical pressure where the transition between on- and off-design modes occurs.

2 PRIOR WORK

The global behavior described above is the result of a combination of complex flow features inside the ejector including boundary layers subject to adverse pressure gradients, turbulent mixing layers bounded by near-wall regions, compressibility effects like shock-induced separations, vortex shedding, and recirculating regions. It is because of this complexity that ejector designs and performances have thus far been difficult to characterize and optimize. With the advent of modern computational techniques, new tools for analyzing such flows have become available to overcome the difficulties in predicting ejector flow. However, they are still far from being completely reliable, making experimental validation necessary. Previous studies [3-6] have highlighted the sensitivity of CFD results to the turbulence model used, and no general agreement has been found as to which turbulence models are best for modeling ejector flows. Several authors have shown that discrepancies between CFD and experiments are strongly related to operating conditions [6, 7]. In

particular, it was found that the prediction of MER at off-design conditions is more challenging than at on-design conditions. One way to capture off-design conditions would be to perform more accurate 3D simulations, but very few examples of this can be found in the literature. Pianthong *et al.* [8] performed 3D simulations on an axisymmetric geometry and found results similar to those from 2D simulations. However, they evaluated only one pressure profile at on-design conditions without considering off-design conditions. Bouhanguel *et al.* [9] also performed 3D axisymmetric simulations with different turbulence models. They compared the results with 2D simulations in the case of zero suction flow and found that 3D calculations were in better agreement with the experimental data.

The lack of off-design validation studies in the literature, coupled with the limited comparison of different turbulence models, provides the motivation for this study. The present work compares several 3D simulations to equivalent 2D simulations for the rectangular cross-sectional ejector geometry of interest. Furthermore, four different turbulence models are compared to find the scheme that best reproduces experimental results. This comparison takes into account global parameters (MER and mass flow rates) and also includes an investigation of the sources of the discrepancy between numerical and experimental results.

3 EXPERIMENTAL SETUP

A schematic of the experimental apparatus is provided in Fig. 3. The air supply to the motive nozzle is provided by an industrial Ateliers François compressor (Model CE46B with a capacity of 1320 m^3/hr FAD and motor power of 250 kW). Before entering the ejector, the air accumulates inside a reservoir at ambient temperature and a set pressure of 16.0 bar. The motive stream pressure is then regulated down to the desired inlet pressure with a Bellofram T-2000 pneumatic valve.

Motive pressures at 2.0, 3.5, and 5.0 bar were tested for comparison with computational results, corresponding to different levels of expansion of the motive flow. The suction flow is taken from the ambient for all tested conditions. The outlet of the ejector also leads to the ambient, and a butterfly valve regulates the exit pressure to the desired set point. For each motive pressure, the outlet pressure is increased incrementally from ambient pressure to produce a full characteristic curve like that shown in Fig. 2.

Figure 3 shows the locations of pressure, temperature, and mass flow measurements. Temperature measurements are taken using PT100 RTD temperature probes (uncertainty ± 0.5ºC including DAQ error), while pressure measurements are taken using Endress Hauser and Kistler pressure transducers (uncertainty < ± 300 Pa). Mass flow rates are determined by measuring the air pressure drop across an orifice plate of known dimensions. The values and uncertainties for these measurements are determined according to ISO standard 5167 (uncertainty generally < ± 0.9%). It should be noted that measuring the mass flow rates in this manner introduces pressure losses that change the conditions at the ejector inlets. For this reason, two other pressure transducers are positioned downstream of the motive and suction orifice plates to yield the correct boundary conditions for comparison with CFD results.

As a means of characterizing the ejector in this test setup (which is detailed in the next section), a full set of characteristic curves was generated experimentally as shown in Fig. 4. For this specific curve set, the reservoir pressure was held at 6 bar, and ambient conditions were at 22°C and 1 bar with a relative humidity of 43%.

4 NUMERICAL MODELLING

The ejector test section itself, shown in Fig. 5, is designed to have undistorted visual access with flat front and back Plexiglas windows. For this reason, the ejector has a planar rather than axisymmetric geometry with a rectangular cross-section. The ejector is designed such that at the given height available for visual access, the depth of the cross-section was enough to allow for the same motive jet surface area available for contact with the suction flow as in the equivalent axially-symmetric version of the geometry. This results in a final aspect ratio of the mixing chamber cross-section of ~2. This high aspect ratio may be a cause of differences between experiments and 2D simulations, as discussed later in this study. Major parameters include a throat height and depth of 6.0 and 48.8 mm respectively, with a throat area ratio, $A_{\text{motive inlet}}/A_{\text{throat}}$, of 12.7.

Simulations are performed using a finite volume approach available in the commercial CFD package ANSYS FLUENT v14.5. For each condition, 2D and 3D steady-state simulations are conducted using four different turbulence models: k-ε, k-ε realizable, k-ω SST, and the stress-ω Reynolds Stress Model (RSM). Dry air is used as the working fluid and is assumed to have the properties of an ideal gas. Spatial discretization of both the conservation and turbulence equations are set to be second-order accurate. The convective and diffusion terms are discretized following an upwind and central difference scheme, respectively, and gradients are evaluated using a least square approach. The coupled set of conservation equations (mass, momentum, energy) and the state equation are linearized following an implicit scheme and solved simultaneously with a density-based solver. Turbulence equations are solved successively following a segregated approach. Convergence of the solution is defined by a change in the mass flow imbalance of less than 10^{-6} kg/s for all the turbulence models except for the k-ε realizable and RSM, where the change is taken to be 10^{-4} kg/s because of difficulties with convergence (see Section 6.2). Calculations are stopped

when all residuals are stable and reach a value of at least four orders of magnitude less than the initial value.

4.1 Computational domain

The domain for 2D simulations is taken to be that indicated in the shaded area of Fig. 5. 3D simulations use the same 2D projection with a depth from one wall to half of the depth shown in Section A-A, as illustrated in Fig. 6. Therefore, the 3D domain has the capability to account for side wall effects, whereas the 2D geometry does not. A structured mesh is adopted and refined at walls to ensure correct modeling of near-wall flow such that $y+$ is always less than 0.9. Turbulence intensities and viscosity ratios at inlets are prescribed according to the value of fully turbulent pipe flows, and all the walls are assumed to be adiabatic. Grid sizes of 75k and 750k cells are used for 2D and 3D simulations, respectively. Grid dependence is checked for all turbulence models for 2D simulations, and just for the k-ω SST and RSM models for 3D simulations. By comparing each case with a mesh of double the original size, the error in the prediction of the mass flow rate was found to be always < 0.2%. Furthermore, the internal flow field was checked for discrepancies in flow features, as shown in Fig. 7, indicating that there were no notable differences.

4.2 Boundary conditions

The boundary conditions used in the numerical analyses are taken as the exact temperature and pressure values from experiments. It should be noted that the physical locations of the experimental pressure measurements in Fig. 3 are different from what is identified as the beginning of the computational domain in Fig. 5. Furthermore, the pressure boundary conditions required by ANSYS FLUENT are total pressures, whereas static pressures are measured on the experimental test setup. The difference between static and total pressures are estimated using numerical results for the

velocities at the inlet sections while the pressure drop from frictional losses are estimated using correlations from [10]. Adding the two contributions (pressure losses and dynamic pressure), it is found that the maximum difference in pressure between any one boundary and its respective pressure measurement is always less than 300 Pa (the small value is due to the very slow speed of both primary and secondary entering the domain, due to large duct sections). A sensitivity analysis showed that such changes in the pressure at the boundary conditions results in < 0.5% change in predicted mass flow rates. Therefore, these effects are considered negligible.

Finally, as stated in the preceding section, mass flow rates are measured by orifice plates that produce pressure losses proportional to the mass flow rate itself. This affects the boundary conditions at the suction inlet. During off-design operation, the suction flow rate decreases and consequently increases the inlet pressure because of a lower pressure loss across the orifice plate. In this work, it was decided not to apply a constant value of total pressure to all the numerical simulations, but instead to change the boundary conditions according to the value measured in the corresponding experiment. The impact of this choice is discussed in subsequent sections. The exact boundary conditions for each simulated case can be found in Appendix A along with the corresponding numerical and experimental results.

5 TURBULENCE MODELLING

Although the working principle of an ejector is simple, correct numerical prediction of the internal dynamics is dependent on the turbulence model used. At present, no universal turbulence model that can accurately predict all possible flow features is available in the literature. Most models achieve a good level of agreement only for the type of flow for which they were previously

calibrated. Wilcox [11] provides an excellent overview of past and current advances in turbulence modelling.

5.1 The *k*-ε Standard and *k*-ε Realizable Models

Among the models selected for this study, the standard *k*-ε model by Launder and Spalding [12] is by far the simplest and oldest. This model has proven to provide accurate results for free shear layers and attached boundary layers with zero or favorable pressure gradients. However, due to its inability to correctly match the law-of-the-wall in the near-wall region, the performance of this model is unsatisfactory for general boundary layer flows, especially those with strong adverse pressure gradients [11]. The model adopted in this work employs a "two-layer approach" that allows for correct integration of the momentum and energy equations through the viscous sublayer [13]. It does so by dividing the boundary layer into a viscous region near the wall, and a fully turbulent region closer to the freestream. The standard *k*-ε formulation is used in the fully-turbulent region, while a simpler model with only one transport equation for the turbulence kinetic energy is employed in the viscous region [14]. This particular near-wall treatment should improve predictions for general boundary layer applications, including those with adverse pressure gradient effects.

A further known issue of the standard *k*-ε model is related to the specific manner in which turbulent viscosity is defined with the Boussinesq approximation, that is:

$$\mu_t = C \cdot \rho \frac{k}{\varepsilon} \tag{2}$$

where ρ is the density and C is a constant. It has been found in several studies, for example, Moore and Moore [15], that specifying a constant value in Equation 2 can lead to unrealistically high levels of turbulent viscosity in flows with a high shear rate (such as impinging jets, flows approaching

stagnation points, and shock-induced separations). These high levels of μ_t are "not realizable" in real turbulent flow. The *k*-ε realizable model [16] improves upon the standard *k*-ε model by introducing a different formulation of the turbulent viscosity that ensures the "realizability" of the model (see [17] for a rigorous, mathematical definition of the "realizability" concept). The different formulation suggested by Reynolds [18] basically substitutes the constant in Equation 2 with an algebraic function that makes the values of μ_t match those obtained from experiments with various flows. Moreover, the model uses a different formulation for the dissipation rate transport equation, derived from the exact transport equation of fluctuating vorticity [19]. Such a formulation should better represent the spectral energy transfer from large eddies to the small dissipative structures [16].

The *k*-ε realizable model has been extensively validated and improves upon the standard *k*-ε model for a wide variety of flows, including round jets, mixing layers, rotating homogeneous shear flows, channel flows, and boundary layer flows. However, because the modification to the standard *k*-ε model is only valid for high Reynolds numbers, the model cannot be expected to provide any significant improvement in near-wall regions. The near-wall treatment used for this model is the same as the one described above and adopted for the standard version.

5.2 The *k*-ω SST Model

An alternative way to work around the near-wall issues of ε-based models is to adopt a different independent variable in place of the dissipation rate, namely the specific dissipation rate, ω. Indeed, models based on ω have the ability to correctly reproduce the law of the wall without the need for any particular modification. This allows for a simple integration along the boundary layer, and results typically show much better agreement for boundary layer simulations, including those with

adverse pressure gradients [11]. However, despite all recent improvements, ω-based models, and in particular the *k*-ω model from Wilcox [11], generally do not achieve the same level of agreement as the *k*-ε model for free mixing layers. Moreover, they suffer from an exaggerated sensitivity to the free stream value of ω, which can sometimes require a sensitivity analysis in order to find the correct solution. In order to reduce these negative characteristics, Menter [20] devised a method that smoothly blends the two models such that the *k*-ω formulation is used in the near-wall region (viscous sublayer and log layer), whereas the *k*-ε model is active elsewhere (boundary layer outer wake region and free stream). The model is named *k*-ω Shear Stress Transport (SST) [20] and employs a "stress limiter" to comply with the "realizability" requirements. This stress limiter is simply a parameter that limits the eddy viscosity to a maximum value in cases of flows with large strain. Within the *k*-ω SST model, the stress limiter has been calibrated specifically to provide good results for transonic flow up to moderate supersonic speeds. As a result, the model achieves a satisfactory level of agreement with a wide range of flows, including those with adverse pressure gradients and transonic shock waves, as are seen in ejector flows.

5.3 The stress-ω RSM Model

Despite these improvements, models based on the Boussinesq approximation are inherently limited in application. By definition, turbulent viscosity μ_t is affected only by the total turbulent kinetic energy, and not by any of its components. This implies that turbulence is modeled as an isotropic process. Consequently, turbulence models based on the Boussinesq approximation fail to yield reliable results for flows where turbulence is largely anisotropic. Examples include flows with sudden changes in mean strain rate, flow over curved surfaces, rotating and three dimensional flows, and flows in non-circular ducts with secondary flows. In particular, this last type of flow is of relevance in this work because the ejector under consideration has a rectangular cross section.

The model adopted in this work is the Wilcox stress-ω RSM [11]. It is very similar to the classic Launder-Reece-Rodi model [21], but differs from commonly-used ε-based RSMs because it employs the ω equation to define dissipation of turbulence kinetic energy. This is justified because of the strong influence of the dissipation equation on the near-wall behavior of the model. RSMs based on the ε equation fail to predict the law of the wall satisfactorily, and the adoption of complicated viscous damping functions make the equations very stiff. By contrast, models based on ω are able to correctly reproduce the law of the wall and are thus easily integrated throughout the viscous sublayer [11].

5.4 Compressibility correction

Ikawa [22] and Maydew and Reed [23] were the first to document the decrease in mixing-layer spreading rate for flows at high Mach numbers. Although the effect has been known for a long time, no convincing theoretical explanation has been given to date, and turbulence models predict this decrease empirically (see Smits and Dussauge [24] or Gatsky and Bonnet [25] for more details). For ω-based models, Wilcox [26] proposes a correction to the turbulence kinetic energy equation based on the turbulent Mach number:

$$M_t = \frac{\sqrt{k}}{a} \tag{3}$$

where a is the speed of sound. This correction reduces the mixing layer entrainment by increasing the dissipation of turbulence kinetic energy through so called dilatation-dissipation [27]. This correction has demonstrated improved accuracy for compressible mixing layers. However, the use of this correction can negatively affect predictions for wall boundary layers at transonic and

supersonic speeds, and is especially detrimental for ε-based models [11]. Because of this, the application of the correction was carefully evaluated.

From inspection of CFD results, the maximum values of turbulent Mach number were checked to understand the impact of compressibility on mixing layers. As shown in Fig. 8, peaks of turbulence Mach number are found in the middle of the shear layer where production of k is more intense. Nonetheless, values of these peaks inside the mixing layer were always less than 0.25. This value was found by [11] to be the threshold for compressibility to have any impact on the mixing layer. Consequently, the effect of compressibility is expected to be limited and no correction is used in the present simulations.

6 RESULTS AND DISCUSSION

6.1 Overview

To best assess the accuracy of 2D and 3D simulations, three experimental characteristic curves at motive pressures of 2.0, 3.5, and 5.0 bar are compared with numerical results. Figures 9 through 12 show this comparison for the four different turbulence models described in the previous section: k-ε, k-ε realizable, k-ω SST, and the RSM. Tables 1 and 2 show the differences between the predictions of each of these models and the data. In Table 1, differences are reported as mean values for on- and off-design regimes, whereas in Table 2, they are summarized separately for each motive pressure considered. Appendix A lists all numerical and experimental results for each condition used for comparison. It should be noted that when results for the motive and suction flows are analyzed separately, differences are always larger than the corresponding value of MER. This is due to a compensation of differences when dividing the two quantities and should caution authors from reporting results in terms of MER alone.

From these comparisons, it can be seen that the differences are generally much lower at on-design conditions. Across all 2D and 3D models, the average difference in MER is 2.6% for on-design and 27.8% for off-design operation. When comparing 2D and 3D models, the differences between predictions and data for on-design operation are comparable, but for off-design operation, the 3D models significantly outperform the 2D models with an average difference of 13.9% in comparison to an average difference of 41.7% for 2D. These differences could be due to many factors, among which numerical factors related to the 2D approximations and turbulence modelling, physical factors such as the geometry and wall roughness of the ejector channel, and thermodynamic discrepancies related to condensation effects are explored below.

6.2 Modeling Discrepancies

The 2D simulations performed in the current study exhibit a high average difference at off-design conditions. In particular, many conditions exhibit an anomalous rise in MER before entering the off-design regime. The reasons for this behavior are to be found both in the inherent limits of 2D simulations and in the way the mass flow rates are measured experimentally. The orifice plate positioned at the inlet of the suction line produces a pressure drop that depends on the mass flow rate itself. At off-design conditions, the suction flow decreases and the pressure at the inlet increases. Hence, the boundary conditions at the suction inlet change. Because 2D schemes predict a later transition to the off-design regime than what is seen experimentally, these higher values of suction inlet pressure are applied to simulations that are still in choked conditions, thus resulting in the abovementioned MER increase. This problem is not obvious, or is absent in 3D simulations because they tend to match the position of the critical point with a much higher accuracy, thus allowing for better off-design values. This is likely due to the fact that the 3D model captures wall effects associated with the front and back walls of the test section (in this case, the Plexiglas

windows used for visualization). Indeed, a significant portion of the motive and suction stream momentum is lost due to friction with the walls, thus decreasing both the suction flow entrainment and the critical pressure. These additional losses cannot be captured by the 2D models, thus retarding the transition to the off-design regime and causing the anomalous MER increase.

Whereas switching to 3D calculations dramatically improves the accuracy of simulations, the performances of different turbulence models are generally within a few percentage points of each other. Among the various models, the standard k-ε model usually has the worst agreement with experimental results in terms of mass flow rates. In particular, the difference introduced for the motive mass flow is always the largest among the different models. Nevertheless, discrepancies are reduced as the motive pressure is lowered. In view of the many modifications to the standard k-ε formulation (see section 5), significant improvement would be expected with the use of the k-ε realizable model, but the improvement only occurs to a small degree at higher motive pressures in our simulations. This is most probably due to the fact that the differences for ε-based models are mostly due to inaccuracies in the near-wall dynamics. As mentioned previously, the k-ε realizable model does nothing to improve upon these known issues at the wall in the standard version. Hence, no significant improvement should be expected for the modeling of ejector flows.

The k-ω SST model is globally the most accurate model in terms of mass flow rate predictions. The greater accuracy of the k-ω SST model can be explained by its inherent structure, which was specifically designed to be accurate for both near-wall and free-stream regions, and calibrated to yield better results for transonic to moderate supersonic regimes (see Section 5).

Looking again at Tables 1 and 2, the global performance of the RSM stress-ω model is comparable with that of the k-ω SST model. As mentioned in Section 5, Reynolds stress models have the potential to better capture 3D phenomena due to the specific modeling of each Reynolds

stress. From close inspection of the solution field for various coordinates (e.g. vorticity, total pressure, etc.,) no significant 3D structures or secondary flows are found. This may be caused by the presence of 2 axis of symmetry in our computational domain. Although this choice allow a reduction of computational costs while accounting for all the wall effects, some questions arise as to the ability of capturing 3D flow structures and secondary flows. Setting the symmetry boundary conditions in Fluent is equivalent to specify a “slip wall” (i.e. zero gradients normal to the plane of symmetry). This means computations are still performed on a rectangular channel, although of smaller dimensions. Consequently, simulations with RSM model should be able to capture all the secondary vortical structures which have characteristic dimensions smaller than half the width of the duct. This is the case for many secondary flow observed in rectangular channel (see Wilcox2006 chapter 6). The absence of any such structure in the numerical results may indicate that turbulence anisotropy plays a minor role in the rectangular geometry considered here. This could also explain why the difference for the RSM model is in line with those of the other models based on the Boussinesq approximation.

Nevertheless, it should be mentioned here that for many of the off-design conditions simulated with the RSM model, steady convergence was not attained. This could be due to the complexity of the model (seven transport equations for 3D calculations and five for 2D), and high grid resolution near the wall. The significant refinement at the wall, necessary for wall-resolved simulation, implies that a wide range of different turbulence scales are captured, from large to very small. This results in increased stiffness of the equations that demands very small time steps to resolve the smallest scales and avoid numerical instabilities. Small time steps, in conjunction with fine grid elements, may cause the model to capture any unsteady behavior (note that all calculations were performed using time marching techniques). This is particularly true at low motive pressures and at significantly off-design conditions where substantial unsteady flow effects can occur. As an

illustration of this effect, Fig. 13 shows a sample flow field using the RSM model at a deep off-design condition (P_{motive} = 2.0 bar, P_{outlet} = 1.0 bar). It can be seen that a shock-induced separation is formed inside the primary nozzle. This, in turn, causes shedding phenomena that are captured by this model, likely preventing any steady convergence of the simulation. One way to overcome this problem is to artificially smooth the simulation by adopting a more diffusive scheme or less refined grid. Hence, a more uniform and less refined grid, but with the same number of nodes, was used for the RSM calculations to achieve steady convergence. Results presented in Tables 1 and 2 correspond to the values obtained with this modified mesh. Although discrepancies with the original grid were found negligible for all global parameters (at least by comparison with the few on-design cases that converged with the original mesh), local results for the RSM model should be considered with some caution when compared with other turbulence models, in that node distribution along the computational domain is different.

6.3 Geometry, NXP, and Wall Roughness Effects

Tables 1 and 2 show that the difference in motive mass flow rate is about the same for all 2D and 3D turbulence models. This seemingly systematic difference is an indication of possible discrepancies between the simulated geometry and real experimental geometry, especially at the primary nozzle throat. As seen in previous work [28] with the same test setup, motive mass flow rate differences were always ~8%. A physical check of the real geometry shows small discrepancies compared with reported values [28]. As such, a new corrected geometry (shown in Fig. 5) is used to conduct the numerical simulations in this study. The difference with the previous nozzle throat are small: the throat under consideration here is about 0.2 mm smaller in depth and 0.1 mm in height. Nevertheless, even such a small difference produces a significant change in primary mass flow rate of the order of 4%, thus leading to a final difference from experimental values of ~3.5%. Although

smaller than previous investigations, this overestimation could be one of the causes of higher critical pressures found in the numerical analyses. A greater motive mass flow rate translates to increased momentum transfer inside the ejector, thus allowing the flow to exit at higher back pressures. Moreover, this overestimation could also influence the entrainment of air from the ambient.

The suction flow is expected to be the most sensitive parameter. As such, the sensitivity to NXP (nozzle exit position, measured from the tip of the motive nozzle to the beginning of the constant-area mixing section) was checked experimentally and shown to be very low, where the variation in suction mass flow rate was of the order of 0.1% per millimeter. Hence, it is unlikely that discrepancies in the position of the nozzle play any role in determining the numerical difference in the suction mass flow rate. As for the impact of wall friction, data summarized in Table 2 show that differences increase with motive pressure, regardless of the turbulence model selected. This suggests that friction losses may contribute to these differences because velocities and friction losses grow as the primary pressure increases. Indeed, recent studies by one of the present authors [29] have demonstrated the significant impact of wall friction on the accuracy of numerical schemes. In particular, it is shown that a correct evaluation of the wall roughness is important for accurate prediction of the critical pressure. Consequently, a sensitivity analysis was conducted with the *k*-ω SST model to study the effect of wall friction on the accuracy of numerical simulations.

Surface roughness values for aluminum are generally between 1 and 2 microns, and for Plexiglas [10], between 2 and 10 microns. Two different 2D simulations are performed using conservative roughness values of 10 and 20 microns at a motive pressure of 5 bar. The 5 bar motive pressure is chosen for the high flow velocities that are likely to accentuate wall friction effects. The results show a <0.2% decrease in the motive mass flow rate in all cases. For the suction stream, the

mass flow rate at on-design conditions decreases by 0.5% for 10 micron roughness, and 0.9% for 20 micron roughness, with respect to the smooth wall case. The greatest changes are observed for the suction flow at off-design conditions. When increasing surface roughness, the effective increase in pressure losses pushes the critical point to lower outlet pressures. This leads to a decrease in the suction mass flow rate of up to 4.5% and 8.7% for a roughness of 10 and 20 microns, respectively (when in the choked regime, only the friction between the inlet and choking location contributes to the decrease in mass flow rate).

Although these changes cannot be considered negligible, the roughness of the actual walls is unknown. Moreover, it is not possible to define wall roughness for ε-based turbulence models when a two layer approach is used (see Section 5). Therefore, all simulations are performed employing the smooth wall boundary condition in order to conduct an unbiased comparison between different schemes. In conclusion, it should be noted that these results confirm the importance of wall effects, a feature that is partly captured in the 3D simulations.

6.4 Condensation

The presence of condensation in the flow is another candidate for the observed differences between experimental and computational results. Due to the high expansion ratios in the motive nozzle, thermodynamic equilibrium is not maintained and any water vapor present in the air becomes significantly subcooled. Under such conditions, a “condensation shock” can form at or near the motive nozzle throat, resulting in sudden changes in pressure and temperature from instantaneous localized heat release [1]. After this condensation shock, the flow contains small liquid droplets that may have an effect on suction flow entrainment [4, 30]. Moreover, condensation may alter the thermodynamic conditions of the primary flow at nozzle exit, e.g., by increasing

pressure and temperature and by reducing the Mach number. This can have impact on the subsequent shear layer development and, therefore, on secondary flow entrainment.

For the test conditions considered in this study, the reservoir pressure was kept at 16 bar, and the flow was expanded to either 2.0, 3.5, or 5.0 bar at the motive inlet. Figure 14 reproduces a diagram from Wegener and Mack [1] showing the Mach number at which condensation was first observed inside various nozzles operating with humid air. As can be seen in this figure, the three points referring to the present study at 16 bar reservoir pressure all lie above the data trend of the previous studies, suggesting that there is condensation at the test conditions considered.

To examine the overall effect of condensation on the flow, tests were performed at various levels of humidity of the motive stream. In general, the moisture content of the motive air depends on the pressure and temperature conditions in the reservoir prior to entering the motive nozzle. To increase the moisture content, the reservoir pressure was decreased from 16.0 to 6.0 bar, and then expanded to the desired motive inlet pressure between 2.0 and 5.0 bar. Preliminary tests were run to determine whether altering absolute humidity in this manner would affect MER, but no detectable change was found in either the mass flow rate or critical pressure of the ejector. This may be because, according to Wegener and Mack [1], condensation is always observed after the sonic throat such that the mass flow rate is unaffected by condensation. Furthermore, the presence of water droplets in the motive stream may not affect entrainment because the momentum of the jet is approximatively the same with or without droplets. In any case, the effect of condensation phenomena requires more detailed study with the aid of visualization techniques currently under development by the authors.

7 CONCLUSION

In the present study, numerical and experimental analyses are conducted to evaluate the effectiveness of common numerical techniques when predicting the flow field inside a rectangular air ejector. Three series of experimental curves at different operating conditions are compared with 2D and 3D, RANS, steady, wall resolved, CFD simulations, using four different turbulence models: *k*-ε, *k*-ε realizable, *k*-ω SST, and the stress-ω Reynolds Stress Model.

A comparison of global parameters finds that agreement between numerical and experimental data is very good at on-design conditions. When moving to off-design conditions, 2D simulations tended to miss the critical point and subsequent off-design points, whereas 3D calculations more closely match the experimental results. It is concluded that the friction losses caused by the front and back walls of the ejector test section prevent the motive jet from transferring some momentum to the suction flow, thus reducing ejector MER and decreasing the critical pressure. This effect, which may be accentuated by the small aspect ratio of the geometry under study, can only be captured by 3D calculations, whose results match the experimental curves more closely.

In terms of choosing the best turbulence model for ejector flow modeling, it is found that different models perform differently depending on the specific operating condition. Globally, the *k*-ω SST model performs the best whereas ε-based models are more accurate at low motive pressures. The RSM model shows predictions comparable to those of the *k*-ω SST, but the model suffers from numerical stiffness and convergence issues that make its use inconvenient.

From close inspection of the numerical differences, it is found that the primary mass flow rate is systematically over-predicted. This is likely due to small discrepancies between the real and computational dimensions of the primary nozzle throat. While the difference is not large, this may

affect the prediction of the critical pressure, as well as the estimation of suction flow entrainment. Discrepancies in the nozzle exit position and the presence of water condensation are found to have negligible impact on determining the mass flow rate of the suction stream. In contrast, an exploration of the role of surface roughness showed that this parameter may affect the transition to off-design conditions. Therefore, it is suggested that wall roughness be taken into account in future studies for better estimation of the critical point.

While differences between turbulence models are not so large, it seems obvious that the use of 3D simulations is almost mandatory to achieve reasonable results at off-design conditions, especially for the rectangular geometry considered here. Moreover, to better assess the predictive capabilities of the various models, further experimental studies are planned that can probe the inside of the ejector to obtain more information on the location and effects of condensation shocks and droplet formation on suction flow entrainment.

REFERENCES

1. Wegener, P.P. and L.M. Mack, *Condensation in Supersonic and Hypersonic Wind Tunnels*, in *Advances in Applied Mechanics*, H.L. Dryden and T.v. Karman, Editors. 1958, Academic Press Inc.: New York, N. Y.
2. Matsuo, K., Y. Miyazato, and H.-D. Kim, *Shock train and pseudo-shock phenomena in internal gas flows.* Progress in Aerospace Sciences, 1999. **35**(1): p. 33-100.
3. Bartosiewicz, Y., Z. Aidoun, P. Desevaux, and Y. Mercadier, *Numerical and experimental investigations on supersonic ejectors.* International Journal of Heat and Fluid Flow, 2005. **26**(1): p. 56-70.
4. Hemidi, A., F. Henry, S. Leclaire, J.-M. Seynhaeve, and Y. Bartosiewicz, *CFD analysis of a supersonic air ejector. Part I: Experimental validation of single-phase and two-phase operation.* Applied Thermal Engineering, 2009. **29**(8-9): p. 1523-1531.
5. Hemidi, A., F. Henry, S. Leclaire, J.-M. Seynhaeve, and Y. Bartosiewicz, *CFD analysis of a supersonic air ejector. Part II: Relation between global operation and local flow features.* Applied Thermal Engineering, 2009. **29**(14-15): p. 2990-2998.
6. Bartosiewicz, Y., Z. Aidoun, and Y. Mercadier, *Numerical assessment of ejector operation for refrigeration applications based on CFD.* Applied Thermal Engineering, 2006. **26**(5–6): p. 604-612.
7. Sriveerakul, T., S. Aphornratana, and K. Chunnanond, *Performance prediction of steam ejector using computational fluid dynamics: Part 1. Validation of the CFD results.* International Journal of Thermal Sciences, 2007. **46**(8): p. 812-822.
8. Pianthong, K., W. Seehanam, M. Behnia, T. Sriveerakul, and S. Aphornratana, *Investigation and improvement of ejector refrigeration system using computational fluid dynamics technique.* Energy Conversion and Management, 2007. **48**(9): p. 2556-2564.
9. Bouhanguel, A., P. Desevaux, and E. Gavignet. *3D CFD simulation of a supersonic air ejector*. in *International seminar on ejector/jet-pump technology and application*. 2009. Louvain-la-Neuve, Belgium.
10. Idelchik, I.E., *Handbook of Hydraulic Resistance*. 3rd Edition ed2008: Jaico Publishing House.
11. Wilcox, D.C., *Turbulence Modeling for CFD*2006, La Canada, California: DCW Industries, Inc.
12. Launder, B.E. and D.B. Spalding, *Lectures in Mathematical Models of Turbulence*1972, London, England: Academic Press.
13. Roques, J.-F. and J.R. Thome, *Falling Film Transitions between Droplet, Column, and Sheet Flow Modes on a Vertical Array of Horizontal 19 FPI and 40 FPI Low-Finned Tubes.* Heat Transfer Engineering, 2003. **24**(6): p. 40-45.
14. Wolfshtein, M., *The velocity and temperature distribution in one-dimensional flow with turbulence augmentation and pressure gradient.* International Journal of Heat and Mass Transfer, 1969. **12**(3): p. 301-318.
15. Moore, J.G. and J. Moore, *Realizability in Two-Equation Turbulence Models*, in *AIAA*1999: Norfolk, VA.
16. Shih, T.-H., W.W. Liou, A. Shabbir, Z. Yang, and J. Zhu, *A New k-e Eddy Viscosity Model for High Reynolds Number Turbulent Flows.* Computers Fluids, 1995. **24**(3): p. 227-238.
17. Lumley, J.L., *Computational Modeling of Turbulent Flows.* Advances in Applied Mechanics, 1979. **18**: p. 123-176.

18. Reynolds, W.C., *Fundamentals of turbulence for turbulence modeling and simulation*, 1987, Von Karman Institute.
19. Tennekes, H. and J.L. Lumley, *A First Course in Turbulence*1972: MIT Press.
20. Menter, F.R., *Two-equation eddy-viscosity turbulence models for engineering applications.* AIAA Journal, 1994. **32**(8): p. 1598-1605.
21. Launder, B.E., G.J. Reece, and W. Rodi, *Progress in the development of a Reynolds-stress turbulence closure.* Journal of Fluid Mechanics, 1975. **68**(03): p. 537-566.
22. Ikawa, H., *Turbulent mixing layer in supersonic flow*, 1973, California Institute of Technology.
23. Maydew, R.C. and J.F. Reed, *Turbulent mixing of compressible free jets.* AIAA Journal, 1963. **1**: p. 1443.
24. Smits, A.J. and J.-P. Dussauge, *Turbulent Shear Layers in Supersonic Flow*. 2nd ed2006, New York, NY: Springer.
25. Gatsky, T.B. and J.-P. Bonnet, *Compressibility, Turbulence and High Speed Flow*. 2nd ed2013, Oxford, UK: Academic Press.
26. Wilcox, D.C., *Dilatation-dissipation corrections for advanced turbulence models.* AIAA Journal, 1992. **30**(11): p. 2639-2646.
27. Sarkar, S. and L. Balakrishnan, *Application of a Reynolds-Stress Turbulence Model to the Compressible Shear Layer*, 1990, ICASE Report 90-18NASA CR 182002.
28. Little, A.B., Y. Bartosiewicz, and S. Garimella, *Optical Validation of Ejector Flow Characteristics Predicted by Computational Analysis*, in *IMECE*2012: Houston, Texas, USA.
29. Mazzelli, F. and A. Milazzo, *Performance analysis of a supersonic ejector cycle working with R245fa.* International Journal of Refrigeration, 2015. **49**(0): p. 79-92.
30. Al-Ansary, H. and S. Jeter, *Numerical and Experimental Analysis of Single-Phase and Two-Phase Flow in Ejectors.* HVAC&R Research, 2004. **10**(4): p. 521-538.

APPENDIX A

Table A1: Tabulated values of exact boundary conditions applied to computational simulations and the corresponding results.

Pressure conditions [bar]			Turbulence model	mass flow rates [kg/s]				Relative error [%]			
motive	suction	outlet	type	motive	suction	outlet	MER	motive	suction	outlet	MER
5.0	0.974	1.200	*k-ε - 2D*	0.343	0.179	0.522	0.521	4.61	7.82	5.55	3.07
			k-ε realizable - 2D	0.339	0.180	0.519	0.531	3.46	8.63	5.05	5.00
			k-ω SST - 2D	0.339	0.181	0.520	0.533	3.45	9.20	5.24	5.56
			RSM - 2D	0.339	0.180	0.520	0.532	3.46	8.92	5.15	5.27
			k-ε - 3D	0.340	0.177	0.517	0.521	3.75	6.87	4.66	3.01
			k-ε realizable - 3D	0.339	0.176	0.516	0.520	3.50	6.42	4.34	2.82
			k-ω SST - 3D	0.339	0.178	0.517	0.525	3.49	7.54	4.71	3.92
			RSM - 3D	0.340	0.176	0.516	0.519	3.587	6.44	4.40	2.75
			exp	0.328	0.166	0.494	0.505	0.000	0.00	0.00	0.00
	0.974	1.700	*k-ε - 2D*	0.343	0.179	0.522	0.521	4.54	8.12	6.07	3.42
			k-ε realizable - 2D	0.339	0.180	0.519	0.531	3.39	8.93	5.57	5.36
			k-ω SST - 2D	0.339	0.181	0.520	0.533	3.37	9.50	5.75	5.92
			RSM - 2D	0.339	0.180	0.520	0.532	3.39	9.21	5.67	5.63
			k-ε - 3D	0.340	0.177	0.517	0.521	3.68	7.16	5.17	3.36
			k-ε realizable - 3D	0.339	0.176	0.515	0.519	3.43	6.58	4.81	3.05
			k-ω SST - 3D	0.339	0.171	0.511	0.506	3.41	3.81	3.87	0.38
			RSM - 3D	0.340	0.176	0.516	0.519	3.514	6.70	4.90	3.08
			exp	0.328	0.165	0.492	0.504	0.00	0.00	0.00	0.00
	0.994	1.800	*k-ε - 2D*	0.343	0.184	0.527	0.536	4.53	62.52	19.68	55.47
			k-ε realizable - 2D	0.339	0.185	0.524	0.545	3.38	63.49	19.07	58.15
			k-ω SST - 2D	0.339	0.185	0.524	0.544	3.37	63.31	19.01	57.99
			RSM - 2D	0.339	0.186	0.525	0.547	3.38	64.18	19.25	58.81
			k-ε - 3D	0.340	0.163	0.503	0.479	3.67	44.12	14.31	39.02
			k-ε realizable - 3D	0.339	0.152	0.491	0.448	3.42	34.61	11.68	30.16
			k-ω SST - 3D	0.339	0.145	0.484	0.427	3.41	28.11	10.00	23.89
			RSM - 3D	0.340	0.159	0.499	0.469	3.507	41.04	13.40	36.27
			exp	0.328	0.113	0.440	0.345	0.00	0.00	0.00	0.00
	1.003	1.875	*k-ε - 2D*	0.343	0.186	0.529	0.543	4.49	137.66	30.59	127.44
			k-ε realizable - 2D	0.339	0.177	0.516	0.523	3.34	126.24	27.45	118.94
			k-ω SST - 2D	0.339	0.166	0.505	0.490	3.32	112.09	24.70	105.26
			RSM - 2D	0.339	0.161	0.500	0.475	3.34	105.59	23.46	98.94
			k-ε - 3D	0.340	0.114	0.455	0.336	3.63	45.97	12.16	40.85
			k-ε realizable - 3D	0.339	0.110	0.449	0.324	3.38	40.46	10.89	35.87
			k-ω SST - 3D	0.339	0.104	0.444	0.307	3.37	33.04	9.45	28.71
			RSM - 3D	0.340	0.104	0.444	0.308	3.465	33.26	9.57	28.80
			exp	0.328	0.078	0.405	0.239	0.00	0.00	0.00	0.00

Pressure conditions [bar]			Turbulence model	mass flow rates [kg/s]				Relative error [%]			
motive	suction	outlet	type	motive	suction	outlet	MER	motive	suction	outlet	MER
			k-ε - 2D	0.241	0.191	0.432	0.791	4.74	3.65	4.59	-1.04
			k-ε realizable - 2D	0.238	0.190	0.428	0.800	3.26	3.30	3.60	0.04
			k-ω SST - 2D	0.238	0.191	0.429	0.803	3.25	3.68	3.77	0.42
			RSM - 2D	0.238	0.191	0.429	0.802	3.27	3.56	3.73	0.28
	0.969	1.200	*k-ε - 3D*	0.239	0.189	0.428	0.791	3.64	2.48	3.45	-1.12
			k-ε realizable - 3D	0.238	0.189	0.427	0.792	3.28	2.35	3.19	-0.90
			k-ω SST - 3D	0.238	0.189	0.427	0.795	3.27	2.72	3.35	-0.53
			RSM - 3D	0.238	0.188	0.426	0.789	3.38	2.04	3.11	-1.30
			exp	0.230	0.184	0.413	0.800	0.00	0.00	0.00	0.00
			k-ε - 2D	0.241	0.191	0.432	0.791	4.78	3.68	4.66	-1.06
			k-ε realizable - 2D	0.238	0.190	0.428	0.800	3.30	3.33	3.67	0.02
			k-ω SST - 2D	0.238	0.191	0.429	0.803	3.29	3.71	3.84	0.40
			RSM - 2D	0.238	0.191	0.429	0.802	3.31	3.59	3.80	0.27
	0.969	1.320	*k-ε - 3D*	0.239	0.189	0.428	0.791	3.69	2.51	3.53	-1.14
			k-ε realizable - 3D	0.238	0.189	0.427	0.792	3.32	2.36	3.25	-0.93
			k-ω SST - 3D	0.238	0.182	0.420	0.765	3.31	-1.12	1.70	-4.29
			RSM - 3D	0.238	0.188	0.426	0.789	3.43	2.07	3.18	-1.31
			exp	0.230	0.184	0.413	0.800	0.00	0.00	0.00	0.00
3.500			*k-ε - 2D*	0.241	0.192	0.433	0.794	4.80	7.84	6.56	2.90
			k-ε realizable - 2D	0.238	0.191	0.429	0.803	3.32	7.47	5.56	4.02
			k-ω SST - 2D	0.238	0.192	0.430	0.806	3.31	7.87	5.73	4.41
			RSM - 2D	0.238	0.192	0.430	0.805	3.33	7.74	5.69	4.27
	0.972	1.380	*k-ε - 3D*	0.239	0.189	0.428	0.793	3.71	6.57	5.39	2.76
			k-ε realizable - 3D	0.238	0.184	0.422	0.772	3.34	3.37	3.78	0.03
			k-ω SST - 3D	0.238	0.173	0.411	0.729	3.33	-2.41	1.25	-5.55
			RSM - 3D	0.238	0.189	0.427	0.792	3.44	6.14	5.05	2.61
			exp	0.230	0.178	0.406	0.772	0.00	0.00	0.00	0.00
			k-ε - 2D	0.241	0.196	0.437	0.810	4.82	41.09	18.99	34.61
			k-ε realizable - 2D	0.238	0.195	0.433	0.819	3.34	40.60	17.88	36.06
			k-ω SST - 2D	0.238	0.189	0.427	0.793	3.33	36.03	16.14	31.65
			RSM - 2D	0.238	0.195	0.433	0.821	3.35	40.98	18.03	36.41
	0.989	1.455	*k-ε - 3D*	0.239	0.165	0.404	0.692	3.73	19.19	10.04	14.91
			k-ε realizable - 3D	0.238	0.161	0.399	0.675	3.36	15.83	8.54	12.07
			k-ω SST - 3D	0.238	0.153	0.391	0.644	3.35	10.56	6.54	6.98
			RSM - 3D	0.238	0.163	0.401	0.683	3.47	17.36	9.18	13.43
			exp	0.230	0.139	0.367	0.602	0.00	0.00	0.00	0.00
	1.009	1.550	*k-ε - 2D*	0.241	0.134	0.375	0.554	4.79	94.53	26.38	85.64

			k-ε realizable - 2D	0.238	0.126	0.364	0.531	3.30	84.11	22.82	78.22
			k-ω SST - 2D	0.238	0.128	0.366	0.536	3.29	85.83	23.21	79.91
			RSM - 2D	0.238	0.118	0.356	0.495	3.33	71.35	19.88	65.83
			k-ε - 3D	0.239	0.090	0.329	0.378	3.69	31.41	10.92	26.73
			k-ε realizable - 3D	0.238	0.088	0.326	0.370	3.32	28.12	9.87	24.00
			k-ω SST - 3D	0.238	0.087	0.325	0.364	3.31	25.96	9.36	21.92
			RSM - 3D	0.238	0.083	0.321	0.349	3.43	20.98	8.30	16.97
			exp	0.230	0.069	0.297	0.298	0.00	0.00	0.00	0.00
Pressure conditions [bar]			**Turbulence model**	**mass flow rates [kg/s]**				**Relative error [%]**			
motive	**suction**	**outlet**	**type**	**motive**	**suction**	**outlet**	**MER**	**motive**	**suction**	**outlet**	**MER**
2.000	*0.955*	1.000	*k-ε - 2D*	0.139	0.204	0.343	1.462	5.93	8.77	7.91	2.68
			k-ε realizable - 2D	0.136	0.202	0.339	1.482	3.74	7.98	6.54	4.09
			k-ω SST - 2D	0.136	0.194	0.331	1.425	3.72	3.78	4.06	0.06
			RSM - 2D	0.136	0.204	0.341	1.497	3.76	9.04	7.18	5.10
			k-ε - 3D	0.137	0.191	0.328	1.393	4.34	2.04	3.29	-2.21
			k-ε realizable - 3D	0.136	0.190	0.327	1.396	3.71	1.70	2.83	-1.94
			k-ω SST - 3D	0.136	0.175	0.311	1.282	3.70	-6.68	-2.12	-10.01
			RSM - 3D	0.137	0.190	0.327	1.392	3.91	1.55	2.82	-2.28
			exp	0.132	0.187	0.318	1.424	0.00	0.00	0.00	0.00
	0.960	1.061	*k-ε - 2D*	0.139	0.205	0.344	1.469	5.86	15.52	11.80	9.12
			k-ε realizable - 2D	0.136	0.202	0.338	1.480	3.68	14.03	10.00	9.98
			k-ω SST - 2D	0.136	0.188	0.324	1.375	3.66	5.90	5.31	2.16
			RSM - 2D	0.136	0.201	0.337	1.472	3.70	13.45	9.68	9.40
			k-ε - 3D	0.137	0.179	0.316	1.302	4.28	0.86	2.68	-3.29
			k-ε realizable - 3D	0.136	0.177	0.313	1.296	3.65	-0.16	1.82	-3.68
			k-ω SST - 3D	0.136	0.165	0.302	1.211	3.64	-6.72	-1.96	-9.99
			RSM - 3D	0.137	0.181	0.317	1.322	3.85	2.03	3.17	-1.75
			exp	0.132	0.177	0.308	1.346	0.00	0.00	0.00	0.00
	0.970	1.107	*k-ε - 2D*	0.139	0.189	0.328	1.357	5.82	22.56	15.39	15.81
			k-ε realizable - 2D	0.136	0.188	0.324	1.378	3.64	21.88	14.01	17.60
			k-ω SST - 2D	0.136	0.177	0.314	1.299	3.61	14.91	10.22	10.90
			RSM - 2D	0.136	0.191	0.327	1.398	3.66	23.70	15.01	19.34
			k-ε - 3D	0.137	0.153	0.291	1.118	4.24	-0.50	2.16	-4.55
			k-ε realizable - 3D	0.136	0.152	0.288	1.114	3.61	-1.53	1.31	-4.96
			k-ω SST - 3D	0.136	0.147	0.284	1.084	3.34	-4.38	-0.36	-7.47
			RSM - 3D	0.137	0.159	0.296	1.163	3.81	3.07	3.90	-0.71
			exp	0.132	0.154	0.285	1.172	0.00	0.00	0.00	0.00
	0.988	1.171	*k-ε - 2D*	0.139	0.130	0.270	0.936	5.75	27.76	16.27	20.82
			k-ε realizable - 2D	0.136	0.139	0.275	1.018	3.57	36.13	18.71	31.44
			k-ω SST - 2D	0.136	0.143	0.279	1.048	3.54	40.07	20.43	35.28
			RSM - 2D	0.136	0.143	0.280	1.050	3.59	40.48	20.64	35.60
			k-ε - 3D	0.137	0.104	0.241	0.757	4.17	1.83	3.96	-2.25
			k-ε realizable - 3D	0.136	0.102	0.238	0.748	3.54	0.00	2.80	-3.42

		k-ω SST - 3D	0.136	0.103	0.239	0.753	3.52	0.64	3.08	-2.78
		RSM - 3D	0.137	0.108	0.245	0.792	3.74	6.12	5.61	2.30
		exp	0.132	0.102	0.232	0.775	0.00	0.00	0.00	0.00
		k-ε - 2D	0.139	0.052	0.192	0.376	5.71	23.03	11.55	16.38
		k-ε realizable - 2D	0.136	0.057	0.194	0.421	3.53	35.01	12.85	30.41
		k-ω SST - 2D	0.136	0.066	0.202	0.484	3.51	55.20	17.83	49.94
		RSM - 2D	0.136	0.062	0.199	0.457	3.56	46.68	15.76	41.63
	1.000 1.233	*k-ε - 3D*	0.137	0.039	0.176	0.284	4.13	-8.32	2.57	-11.96
		k-ε realizable - 3D	0.136	0.037	0.173	0.269	3.50	-13.92	0.71	-16.84
		k-ω SST - 3D	0.136	0.039	0.175	0.286	3.49	-8.27	2.09	-11.36
		RSM - 3D	0.137	0.043	0.180	0.315	3.70	1.07	4.57	-2.54
		exp	0.132	0.043	0.172	0.323	0.00	0.00	0.00	0.00

Table 1: Mean numerical differences for all turbulence models at on- and off-design operation with respect to experimental data (different regimes are defined with respect to experimental curves).

Dim	*Turbulence model*	*mean relative difference at on-design [%]*				*mean relative difference at off-design [%]*				*global mean relative difference [%]*			
		motive	**suction**	**outlet**	**MER**	**motive**	**suction**	**outlet**	**MER**	**motive**	**suction**	**outlet**	**MER**
2D	*k-ε*	*4.92*	*6.41*	*5.75*	*2.25*	*5.18*	*48.06*	*17.47*	*40.91*	5.08	33.18	13.28	27.10
	k-ε realizable	*3.43*	*6.43*	*4.89*	*2.90*	*3.45*	*47.66*	*16.48*	*42.76*	3.45	32.94	12.34	28.52
	k-ω SST	*3.41*	*5.97*	*4.53*	*2.47*	*3.44*	*46.80*	*15.84*	*41.95*	3.43	32.22	11.80	27.85
	RSM	*3.44*	*6.87*	*5.10*	*3.31*	*3.47*	*46.02*	*16.38*	*41.14*	3.46	32.03	12.35	27.63
3D	*k-ε*	*3.82*	*4.21*	*4.02*	*2.17*	*3.92*	*17.64*	*7.13*	*16.26*	3.88	12.84	6.02	11.23
	k-ε realizable	*3.45*	*3.88*	*3.68*	*1.93*	*3.46*	*15.33*	*5.71*	*14.56*	3.45	11.24	4.99	10.05
	k-ω SST	*3.44*	*4.38*	*3.15*	*3.82*	*3.42*	*13.34*	*4.90*	*13.19*	3.42	10.14	4.27	9.84
	RSM	*3.56*	*3.76*	*3.69*	*2.14*	*3.60*	*14.56*	*6.97*	*11.71*	3.59	10.71	5.80	8.29

Table 2: Mean numerical differences for all turbulence models at different motive pressures with respect to experimental data.

Dim	*Turbulence model*	*mean difference for P_{motive} 2.0 bar [%]*				*mean difference for P_{motive} 3.5 bar [%]*				*mean difference for P_{motive} 5.0 bar [%]*			
		motive	**suction**	**outlet**	**MER**	**motive**	**suction**	**outlet**	**MER**	**motive**	**suction**	**outlet**	**MER**
2D	*k-ε*	*5.81*	*19.53*	*12.58*	*12.96*	*4.79*	*30.16*	*12.24*	*25.05*	4.55	54.03	15.47	47.35
	k-ε realizable	*3.63*	*23.01*	*12.42*	*18.71*	*3.30*	*27.76*	*10.71*	*23.67*	3.39	51.82	14.28	46.86
	k-ω SST	*3.61*	*23.97*	*11.57*	*19.67*	*3.29*	*27.42*	*10.54*	*23.36*	3.38	48.52	13.68	43.68
	RSM	*3.65*	*26.67*	*13.65*	*22.22*	*3.32*	*25.44*	*10.22*	*21.41*	3.40	46.98	13.38	42.16
3D	*k-ε*	*4.23*	*2.71*	*2.93*	*4.85*	*3.69*	*12.43*	*6.66*	*9.33*	3.68	26.03	9.07	21.56
	k-ε realizable	*3.60*	*3.46*	*1.90*	*6.17*	*3.32*	*10.40*	*5.73*	*7.59*	3.43	22.02	7.93	17.97
	k-ω SST	*3.54*	*5.34*	*1.92*	*8.32*	*3.31*	*8.56*	*4.44*	*7.85*	3.42	18.13	7.01	14.22
	RSM	*3.80*	*2.77*	*4.01*	*1.92*	*3.43*	*9.72*	*5.77*	*7.12*	3.52	21.86	8.07	17.72

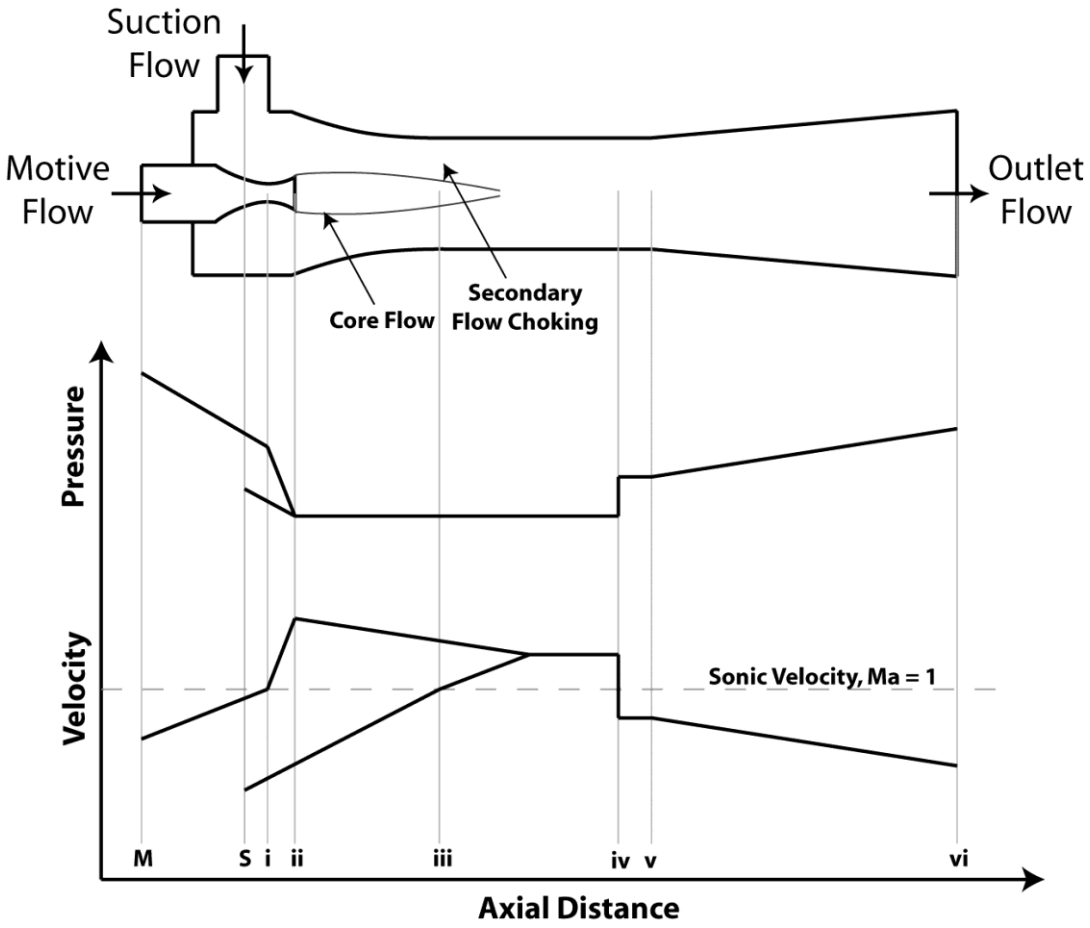

Figure 1. Schematic of ejector with corresponding qualitative pressure and velocity profiles.

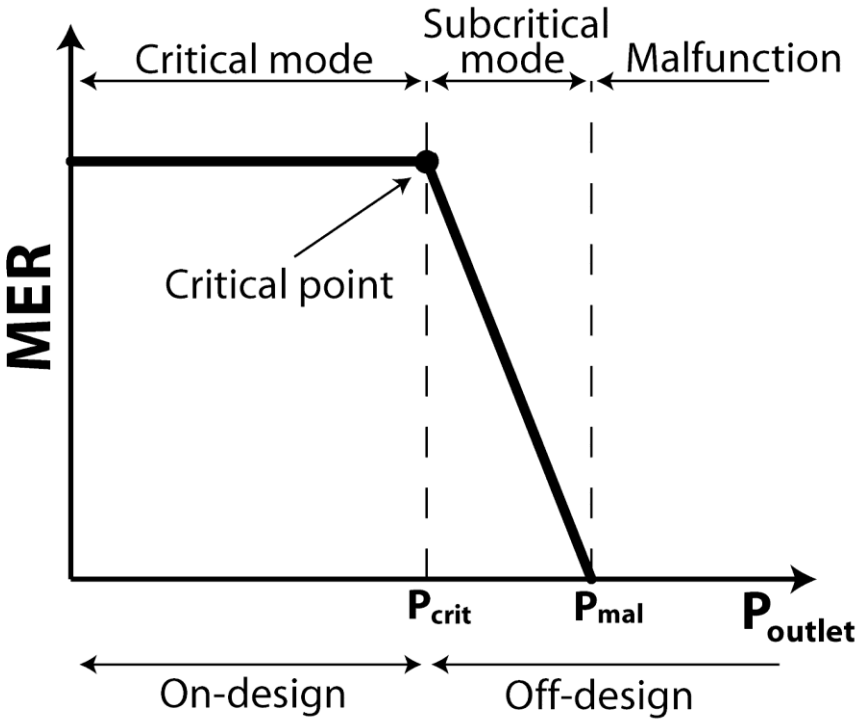

Figure 2. Qualitative ejector characteristic curve at a set motive and suction inlet pressure. On- and off-design regions are labeled, as well as the critical point at the threshold between these two regions.

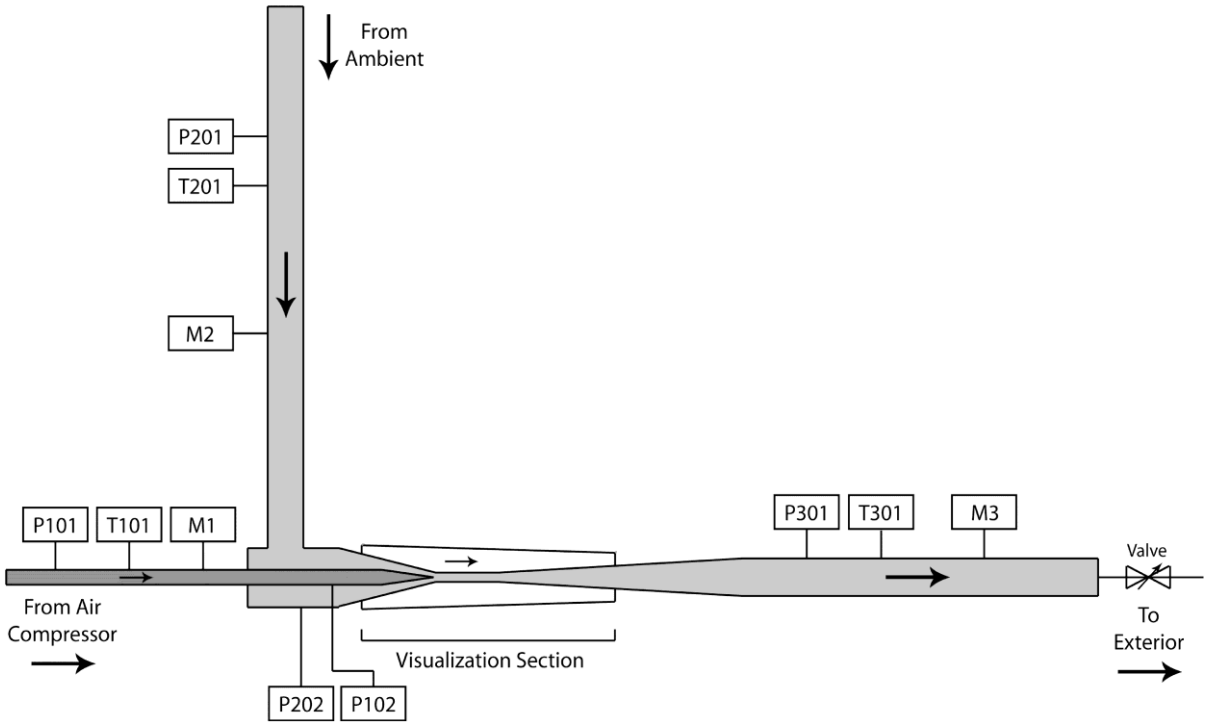

Figure 3. Schematic of overall experimental system indicating locations of pressure and temperature measurements, and orifice plates for mass flow rate measurements.

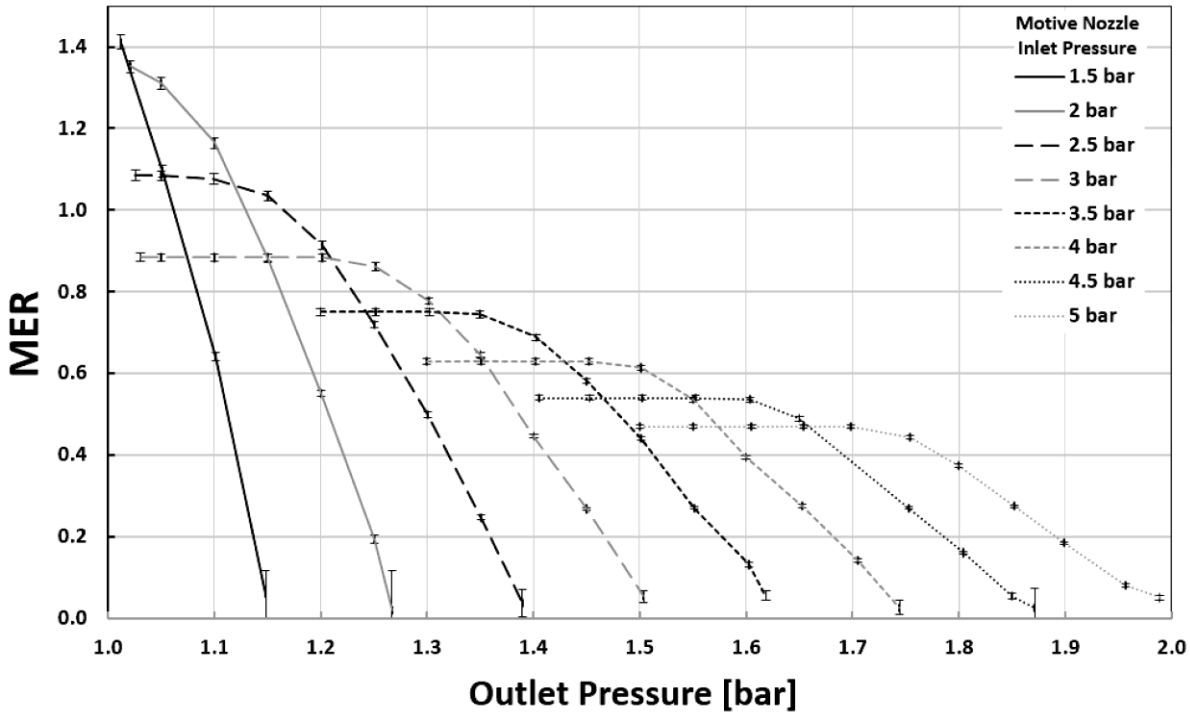

Figure 4. Full set of characteristic curves for the ejector experimental setup. Curves generated using a reservoir pressure at 6 bar, and ambient conditions of 22°C, 1 bar, and 43% relative humidity.

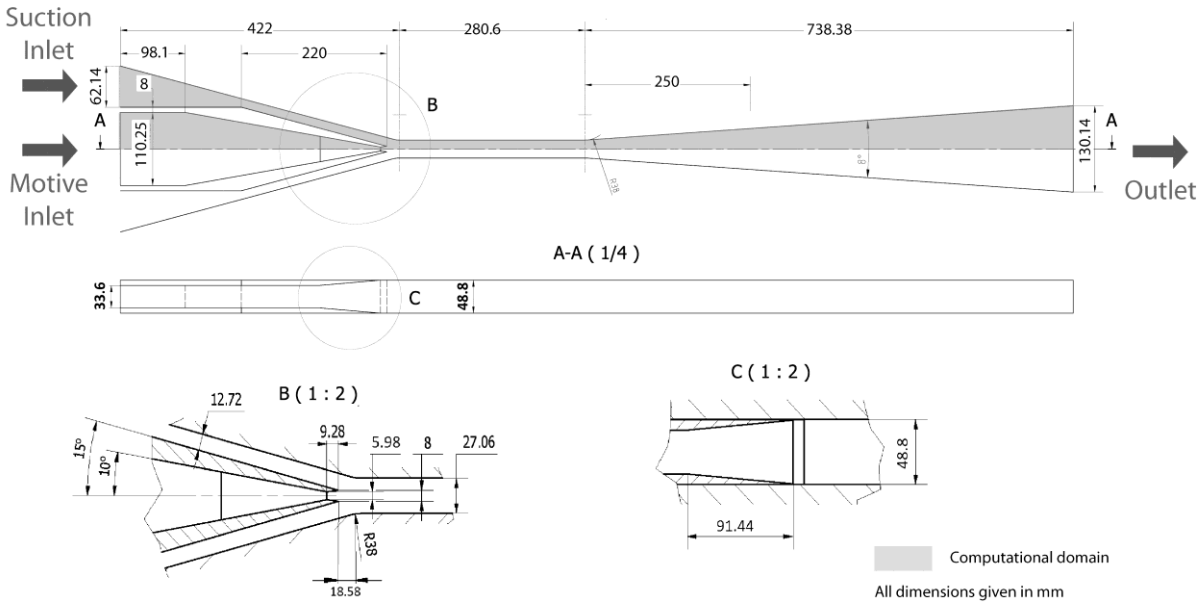

Figure 5. Dimensioned drawing of ejector used for experiments and modeled in numerical simulations. All dimensions are in mm.

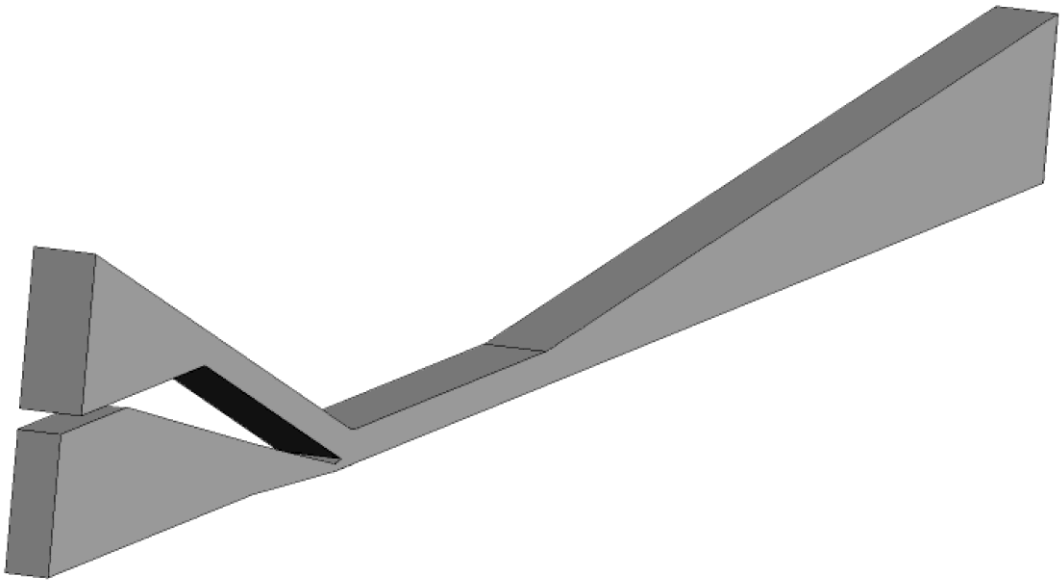

Figure 6. 3D computational domain (one quarter of full domain). The planes of symmetry are the bottom and back walls.

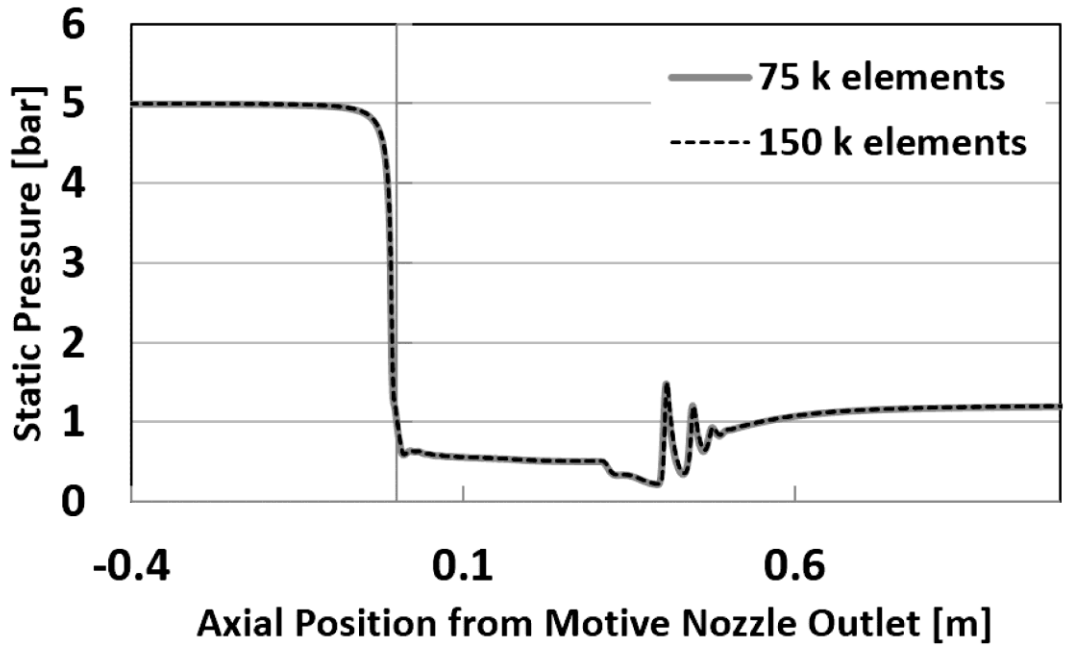

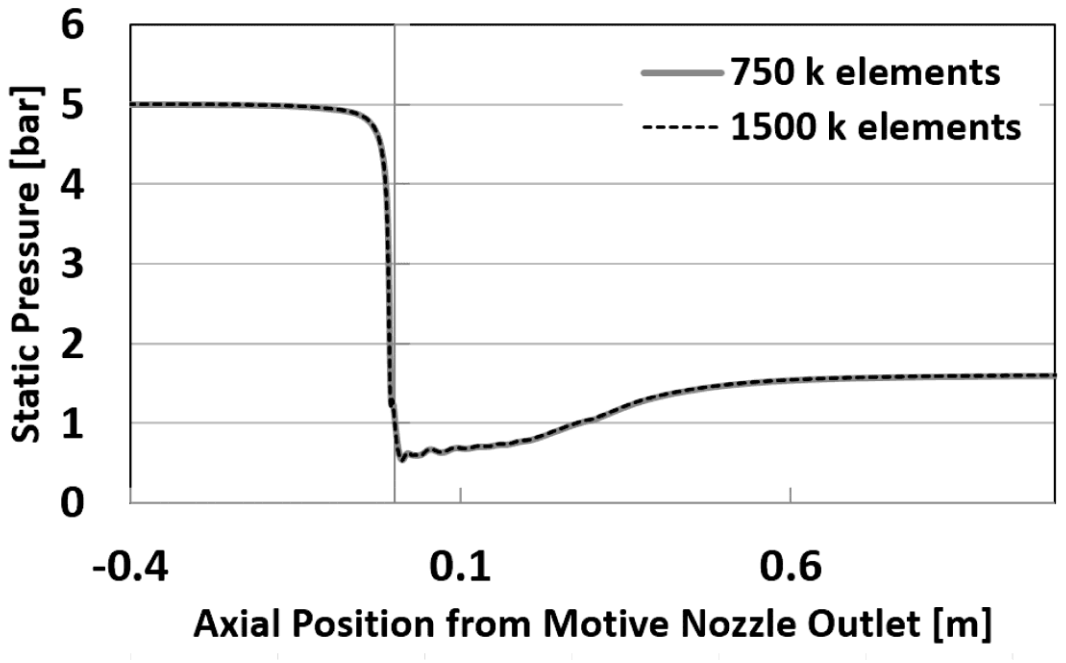

Figure 7. Comparison of axial static pressure profile for grid independence: (top) 2D standard k-ε model for on-design condition at P_m = 5.0 bar, P_s = 1.0 bar, and P_o = 1.2 bar, (bottom) 3D k-ω SST for off-design condition at P_m = 5.0 bar, P_s = 1.0 bar, and P_o = 1.6 bar.

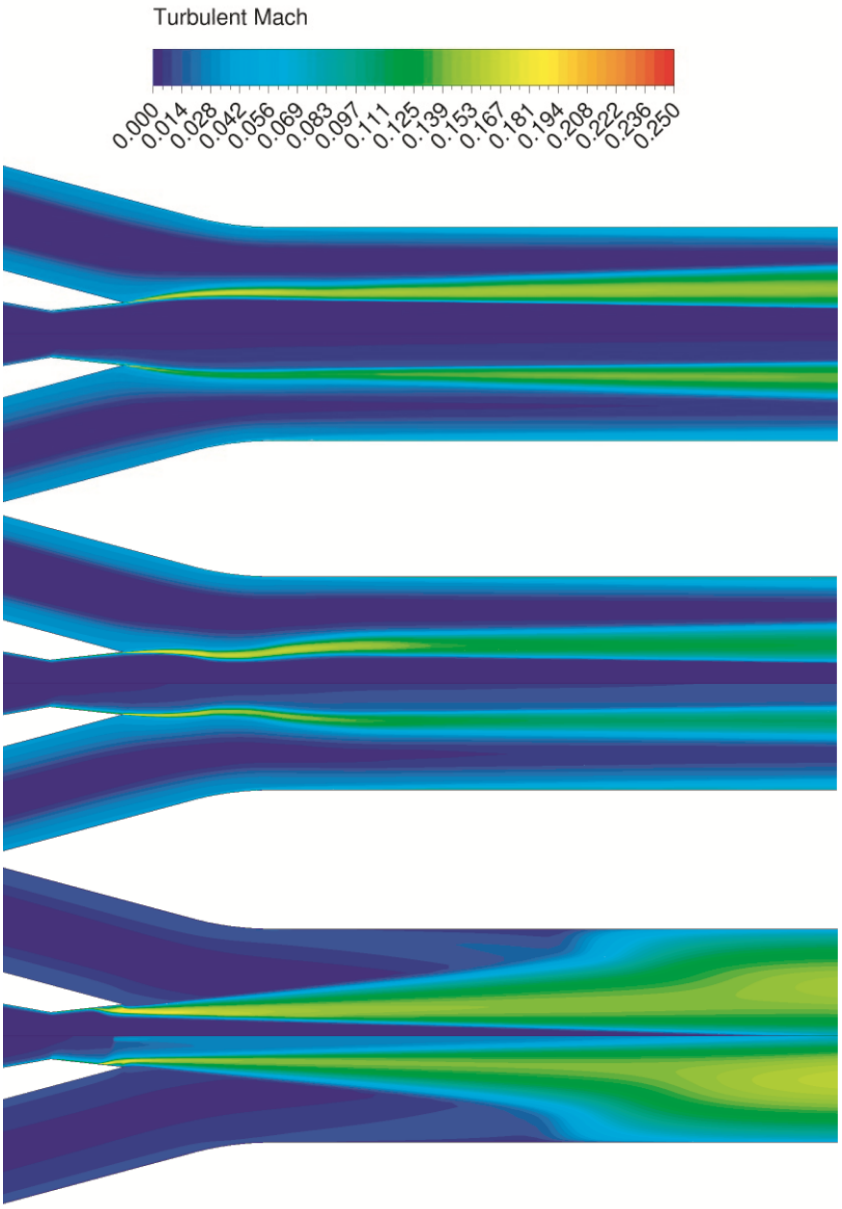

Figure 8. Contours of turbulent Mach number for three different off-design operating conditions: (top) P_m = 5.0 bar, P_s = 1.0 bar, P_o = 1.2 bar, (middle) P_m = 3.5 bar, P_s = 1 bar, P_o = 1.2 bar, (bottom) P_m = 2.0 bar, P_s = 1 bar, P_o = 1.2 bar. Top and bottom halves of each image correspond to k-ω SST and k-ε Realizable turbulence models, respectively.

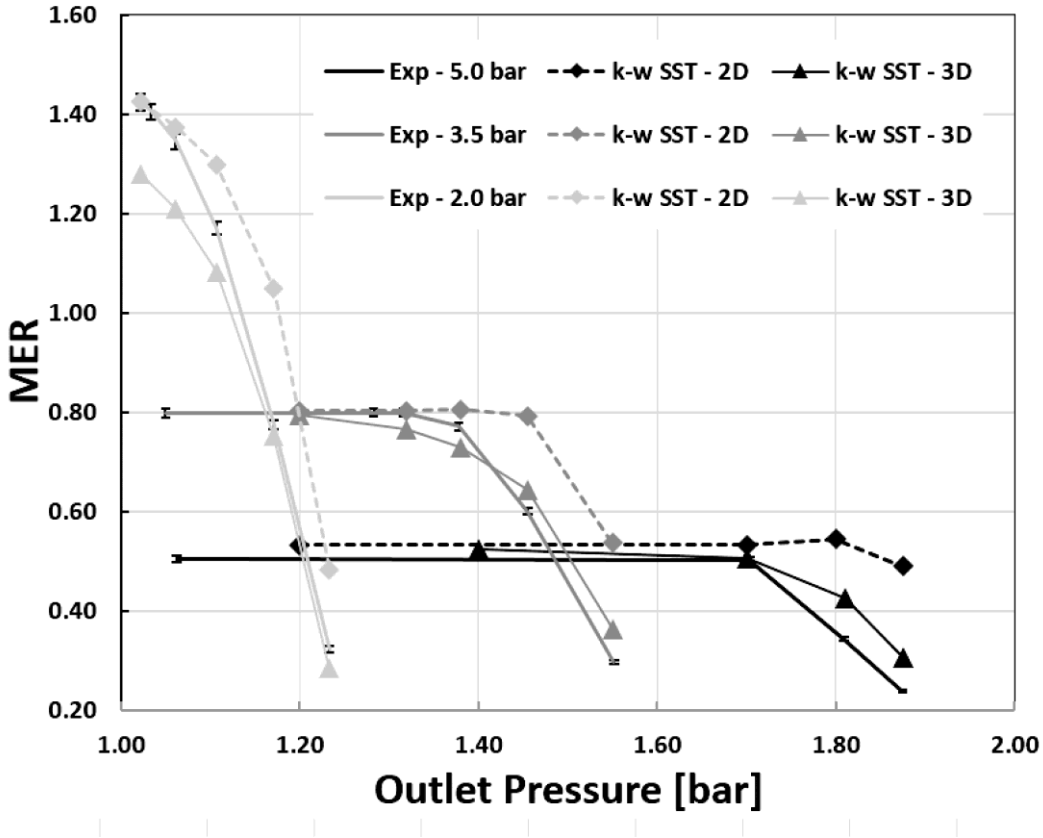

Figure 9. Comparison of experimental characteristics with numerical results from *k*-ω SST model.

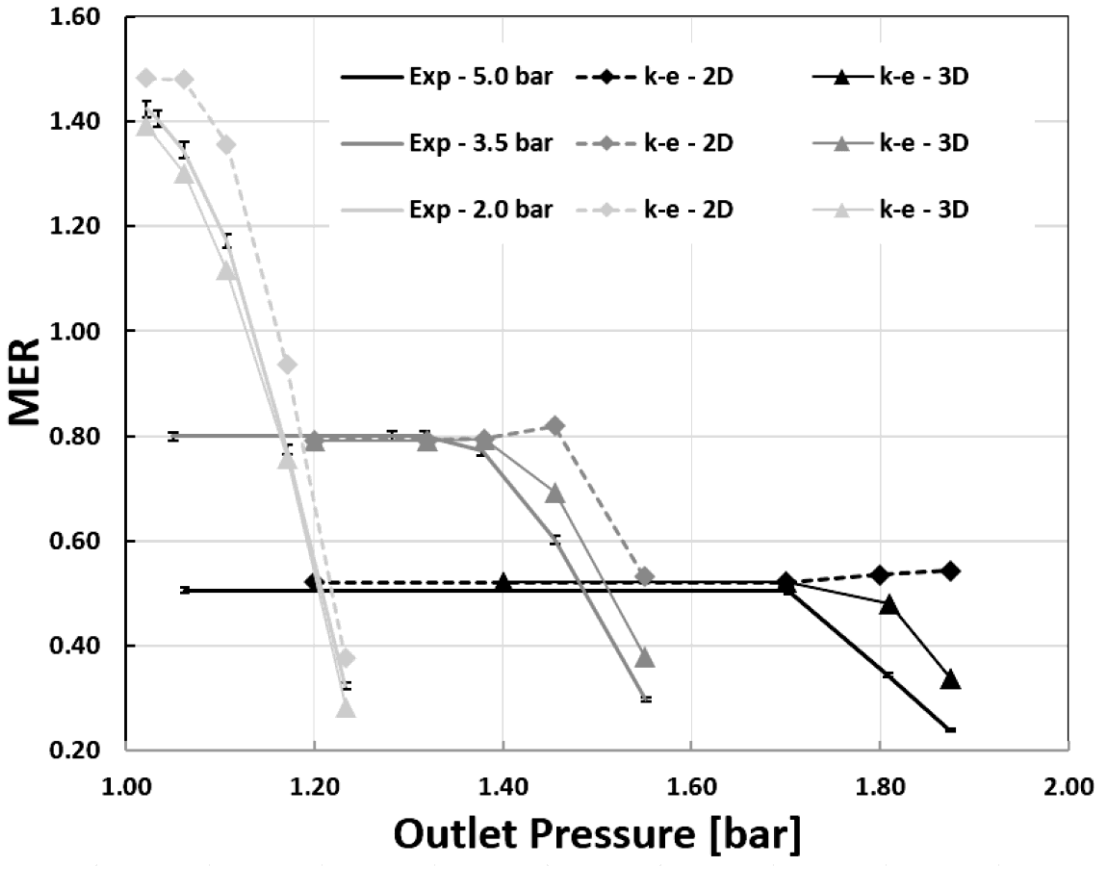

Figure 10. Comparison of experimental characteristics with numerical results from standard *k*-ε model.

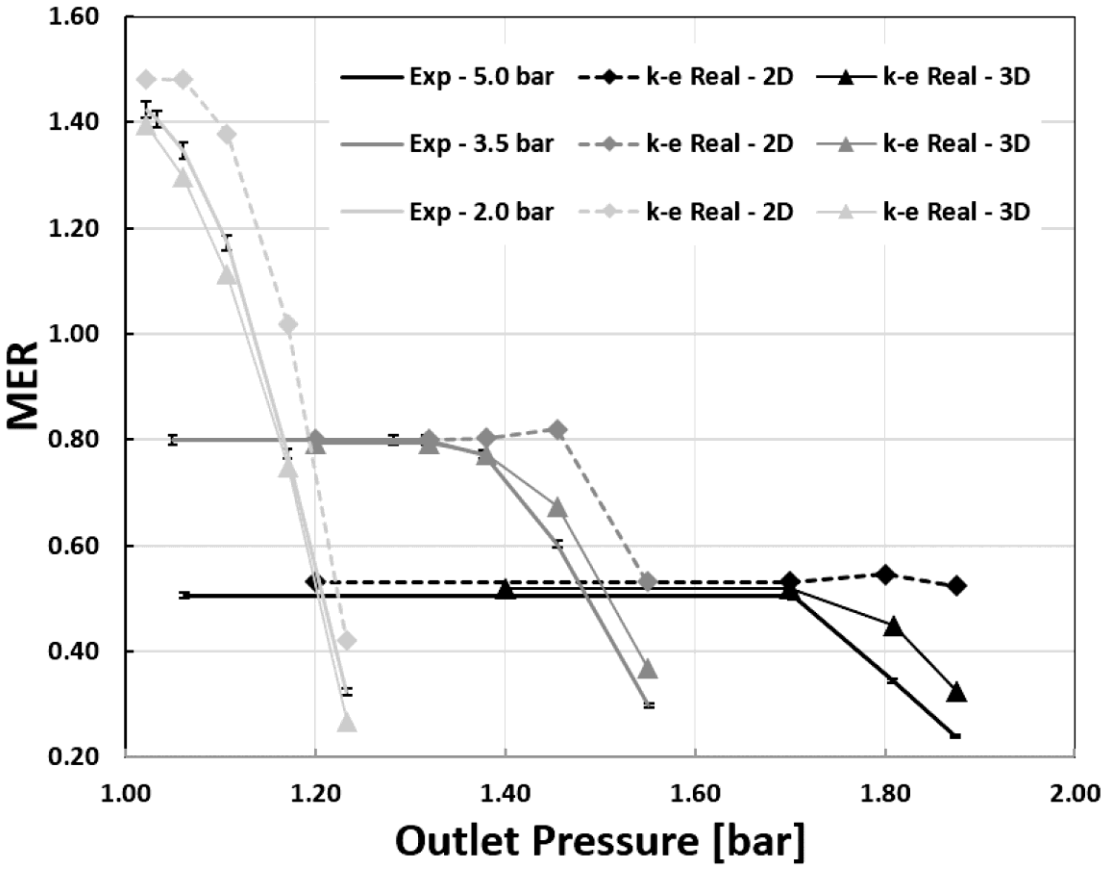

Figure 11. Comparison of experimental characteristics with numerical results from *k*-ε realizable model.

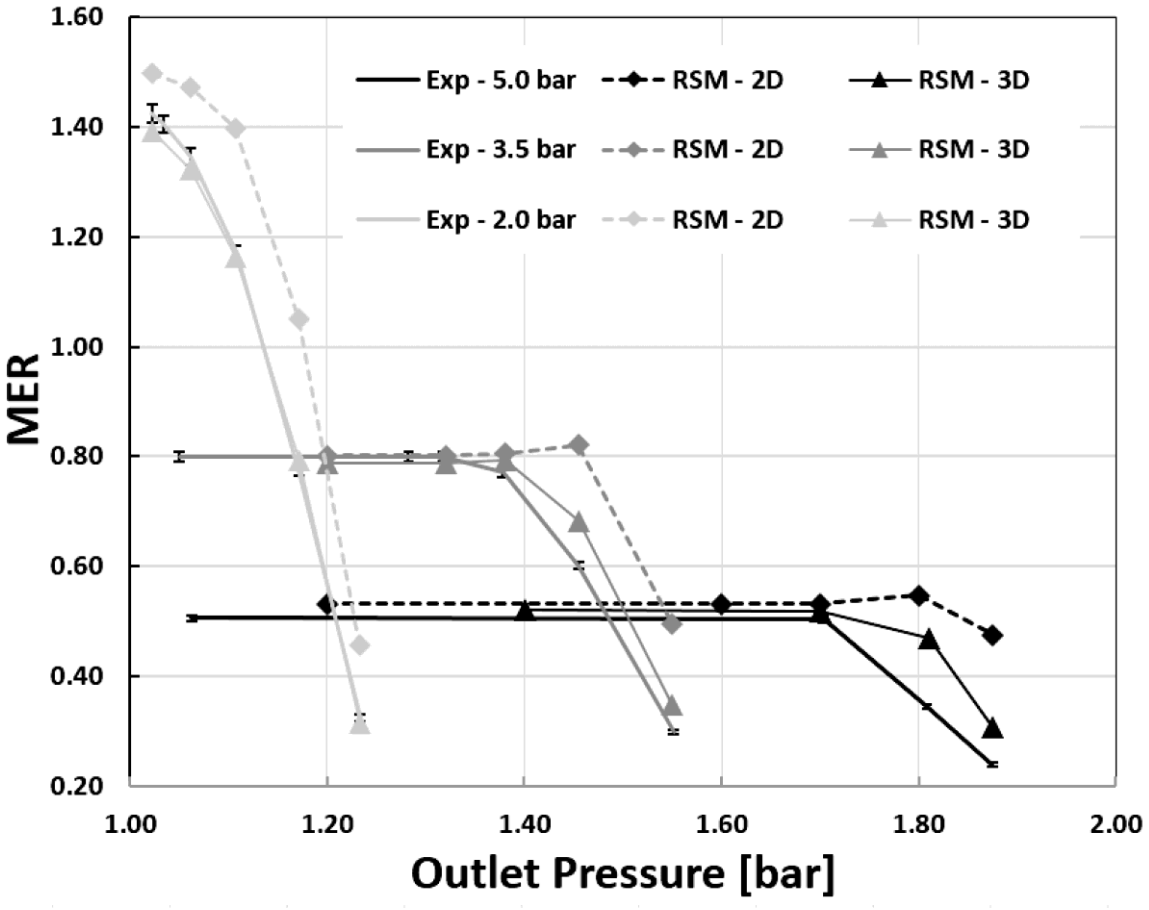

Figure 12. Comparison of experimental characteristics with numerical results from Reynolds stress model. Note that the low Reynolds number approximation was used for all RSM simulations, and 3D simulations were performed using a modified grid to aid in convergence.

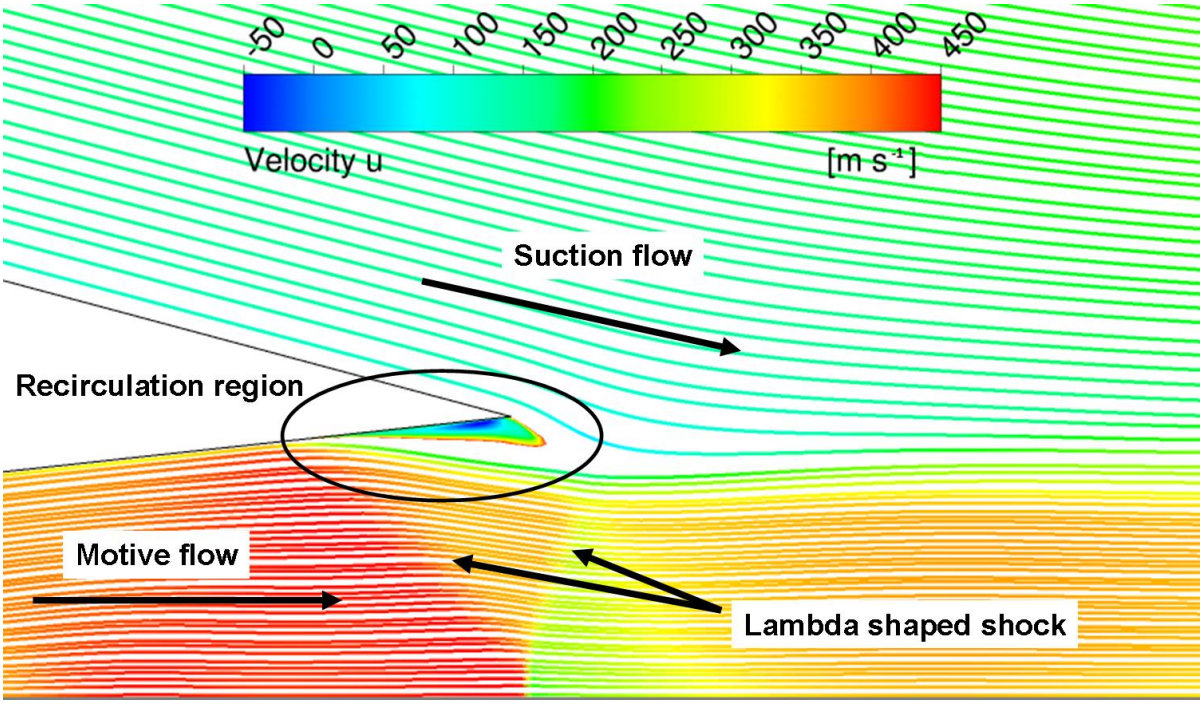

Figure 13. Streamlines and axial velocity contour showing the shock-induced separation at primary nozzle outlet tip. P_m = 2.0 bar, P_s = 1.0 bar, P_o = 1.0 bar.

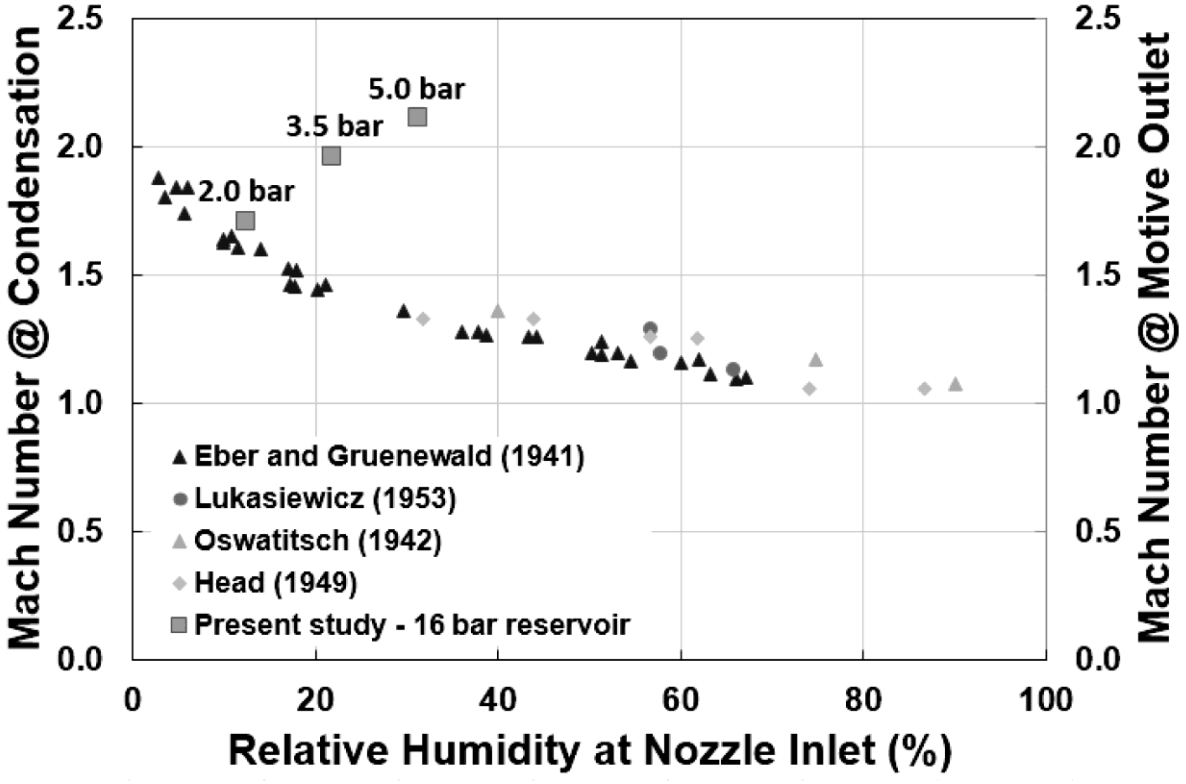

Figure 14. Reproduced data from Wegener and Mack [1] showing conditions of observed condensation in previous studies on humid air flow through nozzles. Data from previous studies references left axis where the Mach number at first observed condensation is plotted against relative humidity at the nozzle inlet. Data from present study references right axis where the Mach number at the motive nozzle outlet (and the maximum velocity in the ejector flow) is plotted against inlet relative humidity for the case of 16 bar reservoir pressure. Note that all points for the present study lie above those from previous studies, indicating a high probability of condensation in the ejector flow.